Micro-Doppler Effect Analysis and Feature Extraction in ISAR Imaging With Stepped-Frequency Chirp Signals

Micro-Doppler Effect Analysis and Feature Extraction in ISAR Imaging With Stepped-Frequency Chirp Signals

Ying Luo, Qun Zhang, *Senior Member, IEEE*, Cheng-wei Qiu, *Member, IEEE*, Xian-jiao Liang, and Kai-ming Li

***Abstract*—The micro-Doppler (m-D) effect induced by the rotating parts or vibrations of the target provides a new approach for target recognition. To obtain high range resolution for the extraction of the fine m-D signatures of an inverse synthetic aperture radar target, the stepped-frequency chirp signal (SFCS) is used to synthesize the ultrabroad bandwidth and reduce the requirement of sample rates. In this paper, the m-D effect in SFCS is analyzed. The analytical expressions of the m-D signatures, which are extracted by an improved Hough transform method associated with time–frequency analysis, are deduced on the range-slow-time plane. The implementation of the algorithm is presented, particularly in those extreme cases of rotating (vibrating) frequencies and radii. The simulations validate the theoretical formulation and robustness of the proposed m-D extraction method.**

***Index Terms*—Hough transform (HT), inverse synthetic aperture radar (ISAR), micro-Doppler (m-D) effect, stepped-frequency chirp signal (SFCS), time–frequency analysis.**

I. Introduction

THE MICROMOTION dynamics of an object or structures on the object may induce frequency modulations on the returned signal, which generate sidebands of the target's Doppler frequency shift, which is called the micro-Doppler (m-D) effect [1]–[4]. Micro-Doppler features can be regarded as a unique signature of an object with movements, providing additional information for the classification, recognition, and identification of the object. On the other hand, the existence of m-D effect may contaminate the inverse synthetic aperture radar (ISAR) image of the main body and bring great difficulties to the image interpretation [1]–[9]. Therefore, it is necessary to separate and extract the m-D signals from the returns of the main body.

Since Chen introduced it into the radar imaging in 2000 [1], the m-D effects, which widely exist in the radar targets (e.g., a helicopter with rotating rotors, a ship with scanning antennas, etc.), have attracted great research attention in accurate target identification. High-resolution time–frequency techniques have been developed to extract these time-varying m-D signatures [3], [5], and the adaptive chirplet presentation for m-D features from the target with rotating parts is studied in [6]. The empirical-mode decomposition is utilized to estimate accurate parameters of the rotating parts and focus the image of the main body in [7]. The image processing algorithms have also been introduced for the separation of the m-D features, such as the Radon transform [8] and the Hough transform (HT) [9], [10]. Furthermore, some literature has reported the application of the m-D effect in automatic target recognition, e.g., the geometrical feature extraction of wheels [11], the micromotion feature extraction of helicopters [5], the urban sensing and indoor sensing [12], the gait and activity analyses of pedestrians [1]–[3], [5], [6], [11], [13], etc.

The m-D signatures describe the fine micromotion features of a radar target. To more effectively exploit the m-D signatures of an ISAR target, the broad-bandwidth transmitted radar signal is necessary to obtain high range resolution. The chirp train with stepped carrier frequencies, i.e., the stepped-frequency chirp signal (SFCS), is one kind of effective signals for obtaining high-resolution downrange profiles of targets. The main advantage of this signal is that the actual instantaneous bandwidth of the radar is quite small, compared to the total processing bandwidth, which allows the transmission of waveforms with extremely wide overall bandwidth without expensive hardware to support the wide instantaneous bandwidth [14]. Thus, this kind of signals can be utilized to introduce imaging capability to existing narrow-bandwidth radar [15]. In contrast to the stepped-frequency signal, the SFCS possesses longer detection distance and lower grating lobes in the range response by means of replacing the fix-frequency subpulses with chirp subpulses [16]. However, due to the frequency-stepped processing, it is sensitive to the radial velocity of the target. When a target contains micromotion structures, the movements of these structures will modulate the high-resolution range profile (HRRP) and exhibit different m-D characteristics from the traditional chirp signal. Most of the present studies focus on the m-D effects with single-frequency signals and chirp signals [1], [6]–[9]. Although the m-D effects with SFCS are briefly discussed in our previous work [17], detailed analyses of the m-D effects and the algorithm for m-D signature extraction are not studied, which motivates this paper.

Manuscript received March 27, 2009; revised June 4, 2009. First published December 4, 2009; current version published March 24, 2010. This work was supported in part by the National Natural Science Foundation of China under Grant 60971100 and Grant 60672032 and in part by the Natural Science Foundation Research Program of Shaanxi Province under Grant 2007F28.

Y. Luo, X. Liang, and K. Li are with the Institute of Telecommunication Engineering, Air Force Engineering University, Xi'an 710077, China.

Q. Zhang is with the Institute of Telecommunication Engineering, Air Force Engineering University, Xi'an 710077, China, and also with the Key Laboratory of Wave Scattering and Remote Sensing Information (Ministry of Education), Fudan University, Shanghai 200433, China (e-mail: zhangqunnus@gmail.com).

C. Qiu is with the Research Laboratory of Electronics, Massachusetts Institute of Technology, Cambridge, MA 02139-4307 USA.

Color versions of one or more of the figures in this paper are available online at http://ieeexplore.ieee.org.

Digital Object Identifier 10.1109/TGRS.2009.2034367

In this paper, we first analyze the m-D signatures and investigate the range profile's migration and wrapping in SFCS in Section II. Particularly, we discuss the m-D effects induced by rotation and vibration in detail and deduce the analytical expressions of the m-D signatures on the range-slow-time plane since the rotating and vibration dynamics are the most common micromotions in radar targets. Then, we propose an algorithm based on an improved HT and time–frequency analysis for the m-D signature extraction in Section III. Due to the range profile's migration and wrapping, the m-D signal of a rotating or vibrating scatterer on the target no longer satisfies the sinusoidal function on the range-slow-time plane. As a result, the HT method for sinusoid detection and estimation in [9] is not suitable for the m-D signature extraction in SFCS. In this section, we construct new HT equations and associate with the time–frequency analysis to extract the m-D signatures of the rotating or vibrating parts with different moving periods and radii. Different from [9], which focuses on the imaging for targets with large-radius and low-frequency rotating parts such as helicopters, this paper mainly deals with the m-D signature extraction for the rotating or vibrating parts with extreme frequencies (very high or very low) and radii that are larger/smaller than the range resolution. Simulations are presented in Section IV, and more discussions are presented in Section V.

In addition, it should be mentioned that the "deramping" method [18] is utilized to synthesize the HRRP for simplicity in this paper. In fact, the analyses of m-D effect and the signature extraction method can easily be extended to imaging systems utilizing other HRRP synthesis methods, such as the time-domain synthesis [19] and the frequency-domain synthesis [20]. Furthermore, considering the small size of general ISAR target and the narrow bandwidth of the chirp subpulses, we assume that the length of target in line of sight (LOS) is shorter than the coarse range resolution of SFCS. Thus, complicated extraction processing of HRRP from redundant data can be avoided, and the analyses of m-D effect are simplified.

II. m-D Effect Analysis

In this section, we first introduce the HRRP synthesis technique with SFCS and then analyze the m-D effects induced by the micromotions, particularly the rotating motion and the vibrating motion.

A. HRRP Synthesis With SFCS

The SFCS transmitted by the radar is made up of a series of bursts, each of which consists of a sequence of chirp subpulses of stepped carrier frequency. Fig. 1 shows the variety of the signal frequency in a burst.

Suppose that the ith subpulse of a burst transmitted by the radar is

$$U_i(t) = u(t - iT_r) \cdot \exp\left(j2\pi(f_0 + i\Delta f)(t - iT_r) + j\theta_i\right), \quad 0 \le i \le N-1 \quad (1)$$

where $u(t) = \text{rect}(t/T_1) \cdot \exp(j\pi\mu t^2)$ is a chirp with μ and T_1 being its frequency modulation slope and time duration,

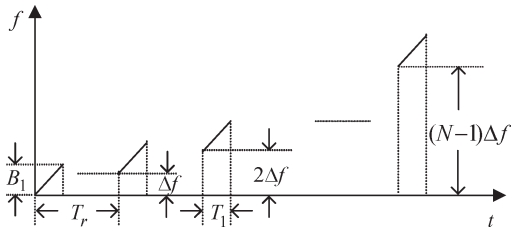

Fig. 1. Frequency variety in a burst of SFCS.

respectively; $f_0 + i\Delta f$ is the carrier frequency; T_r and N denote the subpulse repetition interval and number of subpulses in a burst, respectively; and θ_i is the initial phase. $B_1 = \mu T_1$ stands for the bandwidth of the subpulse, which should be equal to or a bit larger than the stepped frequency value Δf to avoid the interspaces in the synthetic spectrum.

Assuming a target of a point scatterer with unit scattering coefficient, the echo of the ith subpulse from the target is

$$s(t,i) = \text{rect}\left(\frac{t - iT_r - 2R/c}{T_1}\right) \cdot \exp\left(j\pi\mu(t - iT_r - 2R/c)^2\right) \cdot \exp\left(j2\pi(f_0 + i\Delta f)(t - iT_r - 2R/c) + j\theta_i\right) \quad (2)$$

where R is the distance between the target and the radar, and c is the wave propagation velocity. The "deramping" is performed by multiplying the echo signal with the complex conjugate of the reference signal [18], and the reference point can be chosen among the scatterers with the strongest scattering coefficients on target. The reference signal can be written as

$$s_0(t,i) = \text{rect}\left(\frac{t - iT_r - 2R_0/c}{T_{\text{ref}}}\right) \cdot \exp\left(j\pi\mu(t - iT_r - 2R_0/c)^2\right) \cdot \exp\left(j2\pi(f_0 + i\Delta f)(t - iT_r - 2R_0/c) + j\theta_i\right) \quad (3)$$

where R_0 is the distance between the reference point and the radar, T_{ref} is the duration of the reference signal, which is a bit larger than T_1. After the "deramping" processing, it yields

$$\begin{aligned} s_c(t,i) &= s(t,i)s_0^*(t,i) \\ &= \text{rect}\left(\frac{t - iT_r - 2R/c}{T_1}\right) \\ &\quad \cdot \exp\left(-j\frac{4\pi\mu}{c}\left(t - iT_r - \frac{2R_0}{c}\right)R_\Delta\right) \\ &\quad \cdot \exp\left(-j\frac{4\pi}{c}(f_0 + i\Delta f)R_\Delta\right) \cdot \exp\left(j\frac{4\pi\mu}{c^2}R_\Delta^2\right) \end{aligned} \quad (4)$$

where $R_\Delta = R - R_0$. Replacing $(t - iT_r - 2R_0/c)$ by t', applying the Fourier transform to (4) with respect to t', and removing the Residual Video Phase (RVP), one can obtain

$$S_c(\omega,i) = T_1 \text{sinc}\left(T_1\left(\omega + \frac{4\pi\mu}{c}R_\Delta\right)\right) \cdot \exp\left(-j\frac{4\pi}{c}(f_0 + i\Delta f)R_\Delta\right). \quad (5)$$

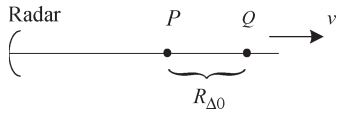

Fig. 2. Nonrigid target with micromotion.

It can be found that the peak value of $|S_c(\omega, i)|$ appears at $\omega = -4\pi\mu R_\Delta/c$, and in fact, it is the coarse range profile of the point target created by the ith subpulse exactly. N subpulses will create N coarse range profiles. Assuming the length of target in LOS to be shorter than the coarse range resolution $c/(2B_1)$, the range profile of the target obtained by chirp subpulse will have only one peak at $\omega = -4\pi\mu R_\Delta/c$. Therefore, keeping $\omega = -4\pi\mu R_\Delta/c$ and taking the Fourier transform of these coarse range profiles with respect to i, one can obtain

$$S(k) = C_n \cdot \text{sinc}\left(k + \frac{4\pi\Delta f}{c} R_\Delta\right) \cdot \exp\left(-j\frac{4\pi f_0}{c} R_\Delta\right) \quad (6)$$

where C_n is a constant. From (6), it can be found that the peak value of $|S(k)|$ appears at $k = -4\pi\Delta f \cdot R_\Delta/c$, i.e., the HRRP is obtained. Divide k by $-4\pi\Delta f/c$, and then, the location of the scatterer in the range can be scaled. Each burst creates an HRRP. By transmitting a number of bursts and taking the Fourier transform to the HRRPs with respect to slow time, the ISAR image of the target can be achieved [17].

B. Micromotion Signatures in SFCS

In many cases, the radar target cannot be regarded as a rigid object, e.g., a helicopter with rotating rotors and a bird with wings beating. When a target contains micromotion parts, the existence of micromotions will affect the synthesis of the HRRP and bring in m-D effect.

As shown in Fig. 2, point P is the reference point, and point Q is a micromotion scatterer with the velocity v relative to P along the LOS. Since the duration of a burst is very short, v can be considered as a constant in burst time approximately. The distance between P and Q at the initial time of a burst is $R_{\Delta 0}$. Due to the movement of Q, in a burst time, R_Δ in (4) should be rewritten as

$$R_\Delta = R_{\Delta 0} + iT_r v. \quad (7)$$

Generally, the displacement of Q in a burst cannot exceed the coarse range resolution. Therefore, (5) can be rewritten as

$$\begin{aligned} S_c(\omega, i) &= T_1 \text{sinc}\left(T_1\left(\omega + \frac{4\pi\mu}{c}(R_{\Delta 0} + iT_r v)\right)\right) \\ &\quad \cdot \exp\left(-j\frac{4\pi}{c}(f_0 + i\Delta f)(R_{\Delta 0} + iT_r v)\right) \\ &\approx T_1 \text{sinc}\left(T_1\left(\omega + \frac{4\pi\mu}{c} R_{\Delta 0}\right)\right) \\ &\quad \cdot \exp\left(-j\frac{4\pi}{c}(f_0 + i\Delta f)(R_{\Delta 0} + iT_r v)\right). \quad (8) \end{aligned}$$

Thus, the HRRP peaks at

$$k = \Phi'(i) = -\frac{4\pi}{c}\Delta f \cdot R_{\Delta 0} - \frac{4\pi}{c} f_0 T_r v - \frac{8\pi}{c}\Delta f i T_r v \quad (9)$$

where $\Phi(i) = -4\pi(f_0 + i\Delta f)(R_{\Delta 0} + iT_r v)/c$ is the phase term in (8). From (9), one can see that the first term on the right side denotes the initial location of the point during the burst time, the second term demonstrates that the location of Q in the HRRP has an offset proportional to v, and the last term is the coupling term between the velocity and the stepped frequency, which is negligibly small, compared with the first two terms (e.g., when $f_0 = 35$ GHz, $T_r = 1$ μs, $i = 1$, $\Delta f = 5$ MHz, $v = 20$ m/s, and $R_{\Delta 0} = 5$ m, the value of this term is only -8.3776×10^{-6}, whereas the values of the first and second terms are -1.0472 and -0.0293, respectively). However, this term may make the peaks of the HRRP seriously expanded, particularly when v is quite large.

Ignoring the last term, (9) is rewritten as

$$k = -\frac{4\pi}{c}\Delta f \cdot R_{\Delta 0} - \frac{4\pi}{c} f_0 T_r v \quad (10)$$

and (10) denotes the peak location of Q in the HRRP. The location of Q in range can be obtained by dividing (10) by $-4\pi\Delta f/c$, i.e.,

$$r = R_{\Delta 0} + f_0 T_r v/\Delta f. \quad (11)$$

Because the HRRP is obtained by N-point Fourier transform, the value range of k is within $[-\pi, \pi]$. If v is too large, k in (10) may exceed this scope, and the peak location of the HRRP may wrap and appear on the other side of the reference point. That is to say, to avoid the wrapping of the HRRP, k must satisfy the following condition:

$$|k| < \pi \quad (12)$$

i.e.,

$$-\frac{c}{4\Delta f} < r < \frac{c}{4\Delta f}. \quad (13)$$

Equation (13) demonstrates that the peak location of the micromotion point is limited to the unambiguous range window. Thus, v must also satisfy

$$-\frac{1}{f_0 T_r}\left(\frac{c}{4} + \Delta f \cdot R_{\Delta 0}\right) < v < \frac{1}{f_0 T_r}\left(\frac{c}{4} - \Delta f \cdot R_{\Delta 0}\right). \quad (14)$$

When the movement of the micromotion point does not satisfy the conditions of (12)–(14), due to the wrapping of the HRRP, the peak location of the micromotion point in the HRRP will be determined by

$$\hat{r} = \text{mod}\left(r + \frac{c}{4\Delta f}, \frac{c}{2\Delta f}\right) - \frac{c}{4\Delta f} \quad (15)$$

where $\text{mod}(a, b)$ returns the remainder of a divided by b.

C. Micro-Doppler Signatures of Rotation and Vibration

In order to more profoundly comprehend the m-D effect in SFCS, we take further analyses of the m-D signatures induced

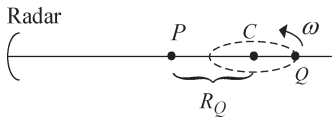

Fig. 3. Target with rotating or vibration scatterers.

by rotating and vibrating parts in a radar target. The rotation and vibration are the most common kinds of micromotions in the radar targets, e.g., a helicopter with rotating rotors, a ship with scanning antennas, and a truck with vibrating surface induced by a running engine.

As shown in Fig. 3, when the micromotion scatterer Q is taking the rotation or vibration motion around C with the rate $\omega_0 = 2\pi\Omega$ and radius ρ, the distance between Q and the reference point P in LOS is expressed as

$$R(t_m) = R_Q + \rho\cos(\omega_0 t_m + \theta_0) \tag{16}$$

where R_Q indicates the distance between the rotating center C and the reference point, θ_0 is the initial phase, and t_m is the slow time, i.e., the transmitting time of each burst. The velocity of the point relative to the radar is

$$v(t_m) = R'(t_m) = -\rho\omega_0\sin(\omega_0 t_m + \theta_0). \tag{17}$$

According to (10), the HRRP of Q peaks at

$$\begin{aligned} k(t_m) &= -\frac{4\pi}{c}\Delta f \cdot R(t_m) - \frac{4\pi}{c} f_0 T_r v(t_m) \\ &= \frac{-4\pi\Delta f}{c}\left(R_Q + \rho\sqrt{1+\omega_0^2 f_0^2 T_r^2/\Delta f^2}\right. \\ &\qquad \left.\times\cos(\omega_0 t_m + \theta_0 + \phi)\right) \end{aligned} \tag{18}$$

where $\phi = \arccos(1/\sqrt{1+\omega_0^2 f_0^2 T_r^2/\Delta f^2})$. When $k(t_m)$ satisfies the condition in (12), the location of the point in range is

$$\begin{aligned} r(t_m) &= R(t_m) + f_0 T_r v(t_m)/\Delta f \\ &= R_Q + \rho\sqrt{1+\omega_0^2 f_0^2 T_r^2/\Delta f^2}\cos(\omega_0 t_m + \theta_0 + \phi). \end{aligned} \tag{19}$$

If $k(t_m)$ does not satisfy the condition in (12), the HRRP will be wrapped, and according to (15), the location of the point in range is

$$\begin{aligned} \hat{r}(t_m) = \mathrm{mod}\Bigg(&R_Q + \rho\sqrt{1+\omega_0^2 f_0^2 T_r^2/\Delta f^2} \\ &\times\cos(\omega_0 t_m + \theta_0 + \phi) + \frac{c}{4\Delta f}, \frac{c}{2\Delta f}\Bigg) - \frac{c}{4\Delta f}. \end{aligned} \tag{20}$$

It can easily be found that (19) is just a subset of (20) under the condition in (12). Therefore, (20) describes the m-D effect in SFCS induced by the rotation and vibration. From (19) and (20), three conclusions can be drawn.

1) When the micromotion parameters of the rotating/vibrating scatterer satisfy the condition in (12), the m-D signatures of the rotating/vibrating scatterer appears to be a sinusoidal curve on the range-slow-time plane. The frequency of the sinusoid is equal to the rotating or vibrating rate of the scatterer. Divide the amplitude of the sinusoid by $\sqrt{1+\omega_0^2 f_0^2 T_r^2/\Delta f^2}$, and then, the radius of the rotation or vibration ρ is obtained.
2) Since $r(t_m)$ in (19) cannot reach its maximum when $R(t_m)$ in (16) reaches its maximum, owing to the phase shift ϕ, it means that, at the moment of the sinusoid maximum, the rotating/vibrating scatterer does not reach the maximum distance from the reference point.
3) When the micromotion parameters of the rotating/vibrating scatterer fail to satisfy the condition in (12), the m-D signature of the rotating/vibrating scatterer appears to be a wrapped sinusoidal curve on the range-slow-time plane. The frequency of the curve is equal to the rotating or vibrating rate of the scatterer.

These characteristics of the m-D effect are different from that in chirp signals. In chirp signals, the sinusoid on the range-slow-time plane would never be wrapped, and the amplitude of the sinusoid is equal to the radius of the rotating or vibrating scatterer [9]. In addition, the sinusoid crest also means that the rotating or vibrating scatterer is reaching the maximum distance from the reference point at the moment. These differences between the SFCS and chirp signal result from the range profile's migration in (10) and the wrapping of the HRRP in (15).

III. Micro-Doppler Feature Extraction

Since the curves on the range-slow-time plane contain the micromotion information of the target, we can extract the m-D signatures by detecting the parameters of these curves. The HT has been recognized as one of the most popular methods for the detection of line segments. It was first introduced by Hough [21] and was later improved to detect analytical curves [22], [23]. The major advantage of the HT is its robustness to noise and discontinuities in the pattern to be detected. In general, the HT can be used to extract the curves' feature with the following basic principle: the parameters $(a_1, a_2, \ldots, a_N)$ are used to represent the curve, and each parameter accumulator simply counts the number of points (x_i, y_i) fitted into the curve equation

$$f(a_1, a_2, \ldots, a_N, x_i, y_i) = 0. \tag{21}$$

The accumulator, which contains the local maxima in the HT space, may correspond to the presence of a curve.

The m-D effects induced by different forms of micromotions appear as different curves on the range-slow-time plane. If the analytical expressions of the curves are obtained, the parameters of the m-D features can be extracted by HT by constructing corresponding transform equations. In the following, we take the rotation and vibration as examples to discuss the m-D extraction algorithm.

According to (20), the parameters $(R_Q, \rho, \omega_0, \theta_0)$ have determined the curve's equation on the range-slow-time plane. We construct the HT equation as follows.

First, (20) is rewritten in the equivalent form

$$\hat{r}(t_m) + \frac{c}{4\Delta f} + M \cdot \frac{c}{2\Delta f} = R_Q + \rho\sqrt{1+\omega_0^2 f_0^2 T_r^2/\Delta f^2}\cos(\omega_0 t_m + \theta_0 + \phi) + \frac{c}{4\Delta f}, \qquad M = 0, \pm 1, \pm 2, \ldots \quad (22)$$

i.e.,

$$R_Q = \hat{r}(t_m) + M \cdot \frac{c}{2\Delta f} - \rho\sqrt{1+\omega_0^2 f_0^2 T_r^2/\Delta f^2}\cos(\omega_0 t_m + \theta_0 + \phi). \quad (23)$$

According to the assumption that the length of the target in LOS is shorter than the coarse range resolution $c/(2B_1)$, i.e., $-c/(4B_1) < R_Q < c/(4B_1)$, and $B_1 \geq \Delta f$, it yields

$$-\frac{c}{4\Delta f} < R_Q < \frac{c}{4\Delta f}. \quad (24)$$

Therefore, (23) can be rewritten as

$$R_Q = \mathrm{mod}\left(\hat{r}(t_m) - \rho\sqrt{1+\omega_0^2 f_0^2 T_r^2/\Delta f^2} \times \cos(\omega_0 t_m + \theta_0 + \phi) + \frac{c}{4\Delta f}, \frac{c}{2\Delta f}\right) - \frac{c}{4\Delta f}. \quad (25)$$

Let $A = \rho\sqrt{1+\omega_0^2 f_0^2 T_r^2/\Delta f^2}$, $\Omega = \omega_0/(2\pi)$, and $\zeta = \theta_0 + \phi$, and we have

$$R_Q = \mathrm{mod}\left(\hat{r}(t_m) - A\cos(2\pi\Omega t_m + \zeta) + \frac{c}{4\Delta f}, \frac{c}{2\Delta f}\right) - \frac{c}{4\Delta f}. \quad (26)$$

Thus, the detection of curves on the range-slow-time plane is transformed to the peak value detection in the parameters (R_Q, A, Ω, ζ) space by utilizing the HT according to (26). The implementation of the HT is given as follows:

Step 1) Set up a discrete accumulator matrix $A_c(R_Q, A, \Omega, \zeta)$, where $R_Q \in [R_{Q\min}, R_{Q\max}]$, $A \in [A_{\min}, A_{\max}]$, $\Omega \in [\Omega_{\min}, \Omega_{\max}]$, and $\zeta \in [\zeta_{\min}, \zeta_{\max}]$ are within the prospective value scales. Zeroize matrix A_c.

Step 2) Apply the HT to all the points on the range-slow-time plane whose module values are greater than a certain threshold, i.e., calculate the curves $(\hat{R}_Q, \hat{A}, \hat{\Omega}, \hat{\zeta})$ in the HT space corresponding to the point $(\hat{r}(\hat{t}_m), \hat{t}_m)$ on the range-slow-time plane according to (26), and then apply

$$A_c(\hat{R}_Q, \hat{A}, \hat{\Omega}, \hat{\zeta}) = A_c(\hat{R}_Q, \hat{A}, \hat{\Omega}, \hat{\zeta}) + 1. \quad (27)$$

Step 3) Search the local maxima in the HT space, and their coordinates $A_c(R_Q, A, \Omega, \zeta)$ are the parameters of the curves on the range-slow-time plane.

The rotating or vibrating rate of the micromotion scatterer $\omega_0 = 2\pi\Omega$ can be obtained from the parameters detected by HT. The rotating or vibrating center can be identified from the parameter R_Q. The radius ρ can also be estimated using the following:

$$\rho = A/\sqrt{1+\omega_0^2 f_0^2 T_r^2/\Delta f^2}. \quad (28)$$

The accuracy of R_Q and A is mainly dependent on the range resolution of the HRRP, and the accuracy of Ω and ζ is determined by the set interval between the adjacent discrete elements in $[\Omega_{\min}, \Omega_{\max}]$ and $[\zeta_{\min}, \zeta_{\max}]$, respectively. The more accurate the Ω and ζ, the more the computer storage and computational time required.

Generally, the algorithm previously presented can extract the m-D signatures from most of the targets with rotating or vibrating parts, such as the horizontal rotors on a helicopter and the rotating antenna on a ship. However, two special situations must be taken into consideration.

A. When $A < c/(4N\Delta f)$

In this situation, the amplitude of the curve is less than half of the range resolution. This situation also widely exists in radar target, e.g., a truck with vibrating surface induced by a running engine or a person with chest fluctuation induced by breathing. When $A < c/(4N\Delta f)$, the curve will appear as a straight line on the range-slow-time plane, and the m-D signatures cannot directly be extracted by HT. Supplementary processing is needed before the implementation of the HT.

Reconsider (8); when letting $\omega = -4\pi\mu R_{\Delta 0}/c$, the HRRP can be synthesized by applying fast Fourier transform (FFT) to the right side of (8) with respect to i. Ignoring the influence of the coupling term between v and i, the result of FFT is approximately obtained, i.e.,

$$S(k) = C_n' \cdot \mathrm{sinc}\left(k + \frac{4\pi\Delta f}{c}R_{\Delta 0} + \frac{4\pi}{c}f_0 T_r v\right) \cdot \exp\left(-j\frac{4\pi}{c}f_0 R_{\Delta 0}\right) \quad (29)$$

where C_n' is a constant. According to (16) and (17), it can be obtained as

$$S(k, t_m) = C_n' \cdot \mathrm{sinc}\left(k + \frac{4\pi\Delta f}{c}R(t_m) + \frac{4\pi}{c}f_0 T_r v(t_m)\right) \cdot \exp\left(-j\frac{4\pi}{c}f_0 R(t_m)\right). \quad (30)$$

Because $A < c/(4N\Delta f)$, $|S(k, t_m)|$ appears as a straight line on the range-slow-time plane; hence, we have the peak location of $|S(k, t_m)|$ at

$$k = -4\pi\Delta f R(t_m)/c - 4\pi f_0 T_r v(t_m)/c \approx \mathrm{C''}_n \quad (31)$$

where C_n'' is a constant. Let $k = C_n''$, and take the derivative to the phase term of the right side of (30) in terms of t_m. Then, the

variance of the instantaneous frequency of $S(k,t_m)|_{k=C_n''}$ with respect to t_m is obtained as

$$l(t_m)=\frac{1}{2\pi}\psi'(t_m)=\frac{2}{c}f_0\rho\omega_0\sin(\omega_0 t_m+\theta_0). \tag{32}$$

It can be found that $l(t_m)$ is a sinusoidal function. Therefore, the m-D signatures can be extracted by analyzing $S(k,t_m)|_{k=C_n''}$ in the joint time–frequency domain first and then utilizing the HT to detect the curve on the time–frequency plane. Similarly, $l(t_m)$ will also be wrapped if $|l(t_m)|>BRF/2$, where the BRF is the burst repetition frequency, i.e., the sample frequency in slow-time domain. Therefore, the curve on the time–frequency plane is depicted as

$$\hat{l}(t_m)=\mathrm{mod}\left(\frac{2}{c}f_0\rho\omega_0\sin(\omega_0 t_m+\theta_0)+\frac{BRF}{2},BRF\right)-\frac{BRF}{2}. \tag{33}$$

Then, the HT equation can be deduced accordingly as

$$\mathrm{mod}\left(\hat{l}(t_m)-A'\sin(2\pi\Omega t_m+\zeta),BRF\right)=0 \tag{34}$$

where $A'=2f_0\rho\omega_0/c$, $\Omega=\omega_0/(2\pi)$, and $\zeta=\theta_0$. Thus, the m-D signature extraction is equivalent to the peak value detection in the parameters (A',Ω,ζ) space.

Since $S(k,t_m)|_{k=C_n''}$ is a sine frequency modulation signal, considering the deficient time–frequency concentration of short-time Fourier transform (STFT) and the cross-term interference in quadratic time–frequency distribution such as Wigner-Ville distribution (WVD) and Smoothing Pseudo WVD, we choose the Gabor transform to analyze $S(k,t_m)|_{k=C_n''}$. Gabor transform has been recognized as one of the best methods to represent pattern signals, owing to its perfect time resolution, frequency resolution, and the absence of cross-term interference [24]. Hence, analyzing $S(k,t_m)|_{k=C_n''}$ with Gabor transform could give many advantages to the following HT processing.

B. When the Rotating or Vibrating Rate Is Extraordinarily High

When *BRF* is given in a radar system, the higher the rotating or vibrating rate, the less the slow-time-domain samplings of the curve in a cycle. If the number of samplings in a cycle is too low, the detection capability of the HT will be depressed, and the parameters of the curve cannot accurately be extracted. Simulation results have demonstrated that the number of samplings in a cycle should be larger than 10–15 to ensure precise detection ability of the HT. For example, in a radar system with $BRF=200$ Hz, the parameters of the curve are difficult to directly be detected from the range-slow-time plane when the rotating or vibrating rate is higher than 20 Hz. (Please refer to the simulations in Section IV-C3.) Furthermore, when the value of v increases, the value of the third term in (9) increases accordingly and more seriously expands the peaks in the HRRP. Therefore, some supplementary processing are also necessary when extracting the m-D signatures of micromotion parts with high rotating or vibration rates, such as the tail rotors on a helicopter or missile.

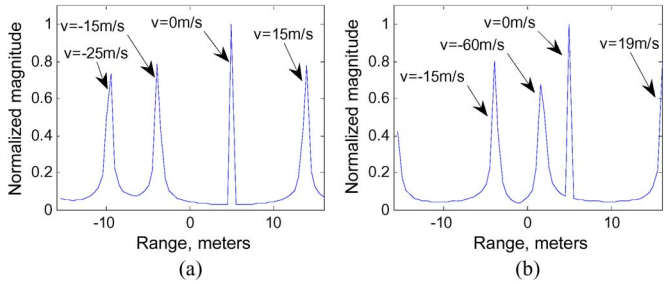

Fig. 4. Range profile's migration and wrapping.

According to the analysis in Section II, the HRRP of the micromotion scatterer is synthesized by taking FFT to (8) with respect to i. When the value of v is quite large, the coupling term between v and i will more significantly affect the HRRP, and the Fourier transform is not suitable to describe the m-D signatures. From (9), the linear relationship between k and i can be observed when assuming v to be a constant approximately in a burst time. Considering that k is the instantaneous frequency of $S_c(\omega,i)$ in (8) at $\omega=-4\pi\mu R_\Delta/c$, $S_c(\omega,i)|_{\omega=-4\pi\mu R_\Delta/c}$ is an approximate linear frequency modulation (LFM) signal. Taking time–frequency analysis to $S_c(\omega,i)|_{\omega=-4\pi\mu R_\Delta/c}$, it will appear as a segment of straight line on the time–frequency plane. Since it is a simple LFM signal, the STFT is competent to analyze it without cross-term interferences.

After taking the STFT to $S_c(\omega,i)|_{\omega=-4\pi\mu R_\Delta/c}$ of each burst, the corresponding time–frequency planes can be obtained, and a new frequency-slow-time plane can be constructed by stitching up these planes in order. On that new plane, the m-D signatures of rotating or vibrating scatterers also appear as the curves depicted by (20), but the slow-time sampling number in a cycle has increased to N times. Therefore, the HT can then be carried out to accurately extract the m-D signatures according to (26).

The aforementioned algorithm is just for the m-D signature extraction of rotation and vibration. Nevertheless, if other micromotions can be depicted by certain analytical expressions, one can also extract their m-D signatures by constructing their respective HT equations.

IV. Simulations

In this section, we verify the theoretical derivation and the proposed m-D extraction method using simulated data. The simulations are composed of three parts: 1) simulations to validate the range profile's migration and wrapping; 2) simulations to validate the m-D signatures induced by rotation; and 3) simulations of m-D signature extraction. Simulation results of vibration are not presented, because it is very close to the case with rotation.

A. Validation of the Range Profile's Migration and Wrapping

The parameters of the transmitted radar signal are $f_0=35$ GHz, $T_r=78.125$ μs, $\Delta f=4.6875$ MHz, $N=64$, and the total bandwidth $B=300$ MHz. Four micromotion scatterers are at the same location with the distance from the reference point $R_{\Delta 0}=5$ m but with different instantaneous velocities. According to (14), it can easily be calculated that $v\in(-36\text{ m/s},18.8571\text{ m/s})$ to avoid the range profile's wrapping.

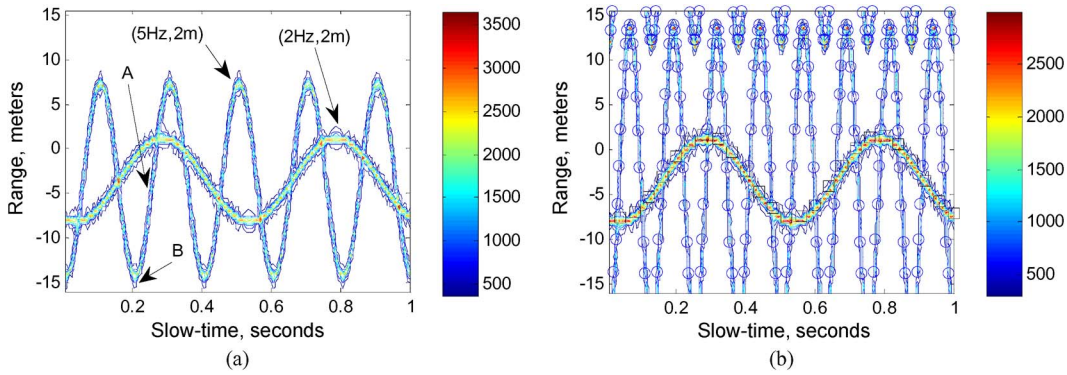

Fig. 5. Micro-Doppler signatures induced by rotation. (a) Curves of the scatterers (2 Hz, 2 m) and (5 Hz, 2 m) on the range-slow-time plane. (b) Curves of the scatterers (2 Hz, 2 m) and (8 Hz, 2 m) on the range-slow-time plane. The "○"-dotted and "□"-dotted dashed curves are determined by (20) when the motion parameters of the scatterer are (2 Hz, 2 m) and (8 Hz, 2 m), respectively.

As shown in Fig. 4, the peak locations of the scatterers in the HRRP are different from each other because of their different instantaneous velocities. In particular, the profile's wrappings are validated in Fig. 4(b). When v is 19 m/s close to the critical point 18.8571 m/s, the peak of the scatterer in the HRRP is split and appears at both sides of the HRRP. When v exceeds the limited value of (14), such as -60 m/s, the corresponding peak of the scatterer is wrapped and appears at the right side of the peak of the scatterer with $v = -15$ m/s. It can also be observed that the peaks are more and more seriously expanded versus the horizontal axis with the increase in $|v|$.

B. Validation of m-D Signatures Induced by Rotation

The parameters of the transmitted radar signals are given as follows: $f_0 = 10$ GHz, $T_r = 78.125$ μs, $\Delta f = 4.6875$ MHz, $N = 64$, $BRF = 200$ Hz, and the total bandwidth $B = 300$ MHz. The range resolution of HRRP is $\Delta_R = 0.5$ m. Two scatterers both rotate around one center with the distance from the reference point $R_Q = -3$ m. The radii are both 2 m, and the initial phase θ_0 are both $\pi/2$. As shown in Fig. 5(a), when the rotating rate is 2 and 5 Hz, respectively, it can be calculated that $|k|_{\max} = 2.6824 < \pi$ according to (18), which satisfies the conditions limited by (12). The magnifying coefficient of the sinusoid's amplitude $\sqrt{1 + \omega_0^2 f_0^2 T_r^2 / \Delta f^2}$ is 2.3209 and 5.3306, respectively. Hence, the amplitude of the sinusoid in Fig. 5(a) is the rotating radius multiplied by $\sqrt{1 + \omega_0^2 f_0^2 T_r^2 / \Delta f^2}$, which is 4.6418 and 10.6613 m, respectively.

In the simulation, the scatterer with a rotating rate of 5 Hz was set to reach the critical position with the largest distance in LOS from the reference point at $t_m = 0.05\,\text{s}, 0.25\,\text{s}, 0.45\,\text{s}, \ldots$. Taking $t_m = 0.25$ s into consideration, although the scatterer has moved to the furthest position in LOS from the reference point, the corresponding sinusoid on the range-slow-time plane has not reached the crest at the moment, such as point A shown in Fig. 5(a). The phase shift ϕ can be calculated as 79.1875° according to (18). As a result, the sinusoid crests at the position indicated by point B in Fig. 5(a).

When the rotating rate of the scatterer (5 Hz, 2 m) increases up to 8 Hz, it can be calculated that $|k|_{\max} = 3.9023 > \pi$. Therefore, the sinusoid will be wrapped as shown in Fig. 5(b). For the sake of validating the correctness of (20), we draw the curves depicted by the equation on the range-slow-time plane using the "○"-dotted and "□"-dotted dashed lines. It can be observed that the curves determined by (20) coincide well with the simulation results.

TABLE I
CURVE PARAMETERS DIRECTLY OBTAINED VIA HT FROM THE RANGE-SLOW-TIME PLANE

Sequence Number	1	2	3	4	5
R_Q	–3	–3	–3	–3	–3
A	4.5	5	4.5	5	17
Ω	2	2	2	2	8
ζ	2.6	2.6	2.7	2.7	2.9

C. Validation of m-D Signature Extraction Algorithm

The parameters of the transmitted radar signals are the same as those in Section IV-B. In this section, the effectiveness of the m-D signature extraction algorithm is validated in Sections IV-C1–IV-C3, and the robustness of the algorithm is discussed in Section IV-C4.

1) Detect Curves Using HT on the Range-Slow-Time Plane Directly Under the Most Common Conditions: Assume that two scatterers are both rotating around one center with the distance from the reference point $R_Q = -3$ m. The radii are both 2 m, and the rotating rates are 2 and 8 Hz, respectively. The initial phase θ_0 are both $\pi/2$. The corresponding curves on the range-slow-time plane have been shown in Fig. 5(b). The parameter pairs (R_Q, A, Ω, ζ) detected by HT are shown in Table I. It can be found that the rotating rates of the two scatterers and the value of R_Q are accurately obtained. The average value of parameter A is about 4.75 and 17 m, respectively. According to (28), the radii of rotating scatterers are 2.0466 and 2.0149 m, which agree quite well with the set value of 2 m.

2) Detect Curves When $A < c/(4N\Delta f)$: Assume that two scatterers rotate around the center with the distance from the reference point $R_Q = -3$ m. The radii are both 0.05 m, and the rotating rate is 2 and 4 Hz, respectively. The initial phase θ_0 are both 0 rad. It can be calculated that $A_1 = 0.1160$, $A_2 = 0.2153$, and $c/(4N\Delta f) = 0.25$, which satisfy $A_1 < c/(4N\Delta f)$ and $A_2 < c/(4N\Delta f)$. Because the amplitudes are smaller than

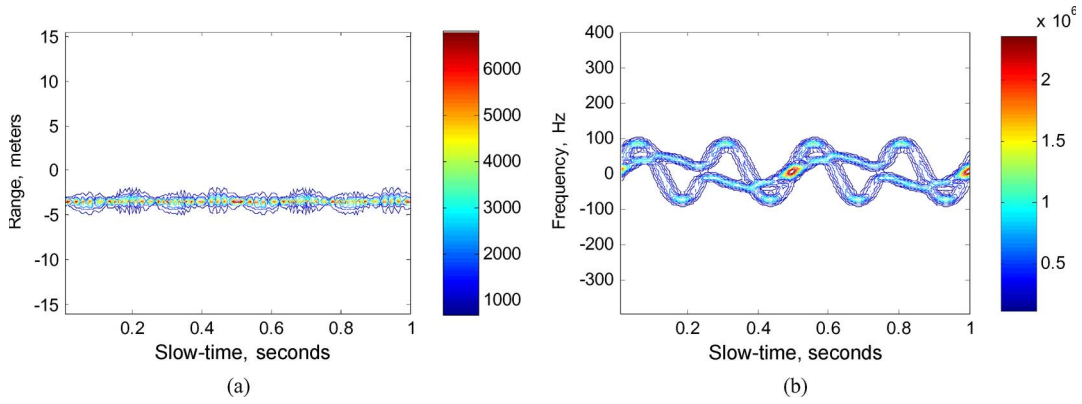

Fig. 6. Micro-Doppler signature extraction when $A < c/(4N\Delta f)$. (a) Curves on the range-slow-time plane appear to approximately be a straight line. (b) Sinusoidal curve obtained by applying the Gabor transform to the row of straight lines.

TABLE II
CURVE PARAMETERS OBTAINED VIA HT WHEN $A < C/(4N\Delta f)$

Sequence Number	1	2	3	4	5	6	7
A'	41	44	45	85	84	83	87
Ω	2	2	2	4	4	4	4
ζ	0.1	0.0	0.0	0.0	0.1	0.0	0.1

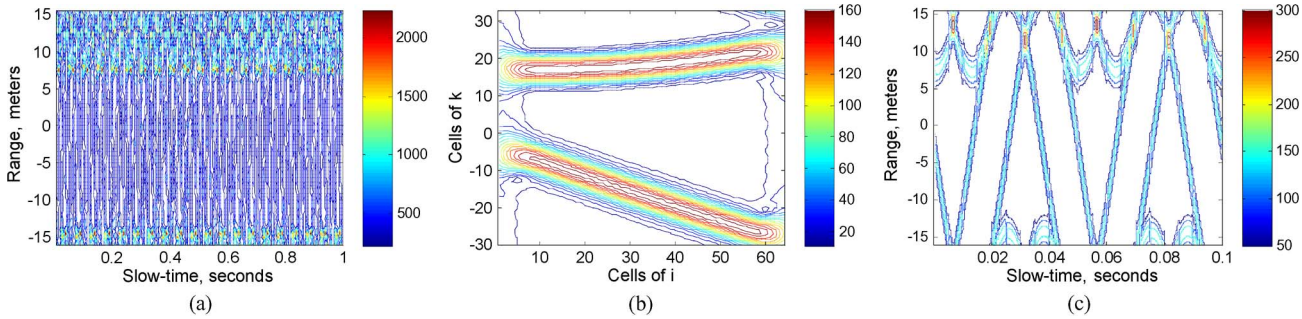

Fig. 7. Micro-Doppler signature extraction when the rotating rate is extraordinarily high. (a) Blurry curves on the range-slow-time plane. (b) STFT result of $S_c(\omega, i)$ in (8) at $\omega = -4\pi\mu R_\Delta/c$. It appears to be segments of straight lines on the time–frequency plane. (c) New frequency (range)-slow-time plane constructed by stitching up the planes of all the bursts in order.

half-range resolution, the curves appear to be a straight line approximately, as shown in Fig. 6(a). In this condition, the HT is unable to detect the parameters from the range-slow-time plane. Extracting the row of straight line, taking interpolations for four times, and then implementing Gabor transform to the row, the sinusoidal curves are obtained as shown in Fig. 6(b). The synthesis window in the Gabor transform is a Gaussian window. The number of Gabor coefficients in time is 100, and the degree of oversampling is 20. Then, the HT can be implemented to obtain the parameters (A', Ω, ζ), and the results are shown in Table II.

It can be observed in Table II that the rotating rates are accurately detected as $\Omega = 2$ and 4 Hz. The average values of parameter A' are about 43.33 and 84.75, respectively. According to (34), the rotating radii are calculated as $\rho = A'c/(2f_0 \cdot 2\pi\Omega) = 0.0517$ m and 0.0506 m, which are quite close to the set value of 0.05 m. In fact, the errors are mainly dependent on the frequency resolution of the Gabor transform.

3) Detect Curves When the Rotating or Vibrating Rate Is Extraordinarily High: Assume that two scatterers both rotate around one center with the distance from the reference point $R_Q = -3$ m. The radii are both $\rho = 1$ m, and the rotating rates are the same at 20 Hz. The initial phase θ_0 is 0 and $\pi/2$, respectively. The magnifying coefficient of the sinusoid's amplitude is $\sqrt{1 + \omega_0^2 f_0^2 T_r^2/\Delta f^2} = 20.9678$, i.e., $A = 20.9678$ according to (28).

The curves on the range-slow-time plane are shown in Fig. 7(a). The curves are very blurry because of the high rotating rates; as a result, the parameters of the curves cannot exactly be detected by the HT from the range-slow-time plane, as shown in Table III. It can be found that the detected parameters fail to fit to the set values.

Fig. 7(b) shows the STFT result of $S_c(\omega, i)$ in (8) at $\omega = -4\pi\mu R_\Delta/c$. It can be seen that $S_c(\omega, i)|_{\omega=-4\pi\mu R_\Delta/c}$ is an approximate LFM signal on the time–frequency plane, i.e., the $i-k$ plane. Stitching up the planes of all the bursts in order, a new frequency-slow-time plane can be constructed, as shown in Fig. 7(c). For clarity of the figure and ease of comprehension, Fig. 7(c) presents just a part of the new plane from 0 to 0.1 s in the slow time, and the frequency

TABLE III
CURVE PARAMETERS OBTAINED VIA HT FROM THE RANGE-SLOW-TIME PLANE WHEN THE ROTATING RATE IS EXTRAORDINARILY HIGH

Sequence Number	1	2	3	4
R_Q	–3	3	3	3
A	21.5	8	6	6
Ω	20	20	20	20
ζ	1.0	0.1	1.9	1.7

TABLE IV
CURVE PARAMETERS OBTAINED VIA STFT AND HT WHEN THE ROTATING RATE IS EXTRAORDINARILY HIGH

Sequence Number	1	2	3	4
R_Q	–3	–3	–3	–3
A	21	21.5	21	21.5
Ω	20	20	20	20
ζ	1.5	1.5	3.1	3.1

axis is transformed to the range axis for consistency with Fig. 7(a).

Thus, the curves in Fig. 7(c) are more obvious, and the HT can be utilized to detect the parameters exactly. The detected parameters (R_Q, A, Ω, ζ) of the two curves are given in Table IV and fit well to the set values.

4) Robustness Discussion: In actual situations, the micromotion parts are always masked by the target's body. As a result, the induced m-D signals are contaminated by the target body's returns. In the processing of m-D feature extraction, these body returns must be considered as "noise," because they will bring in mistakes. Meanwhile, for simplicity, we have assumed the target consists of point scatterers with unit scattering coefficients. However, for a rotating target with a large radius or high frequency in real-world situations, it is highly possible that the backscattering coefficients have time-varying complex values. In the following, we further study the performance of the proposed algorithm in these situations.

SNR: After sufficiently accurate translation compensation, the body scatterers can be considered as micromotion scatterers with zero rotating frequency approximately; therefore, the corresponding curves on the range-slow-time plane or the frequency-slow-time plane appear to be straight lines. According to the difference between the m-D curves and the body's straight lines, a primary and simple noise suppression method is designed as follows: assuming that the data matrix on the range-slow-time plane or the frequency-slow-time plane is $\mathbf{M}$ with $X \times Y$ points, the straight-line-removing processing can be expressed as

$$\mathbf{M}'(x,y) = |\mathbf{M}(x,y)| - \frac{1}{Y}\left(\sum_{y=1}^{Y} |\mathbf{M}(x,y)|\right) \cdot \mathbf{M}_Y \quad (35)$$

where $\mathbf{M}_Y$ is a $1 \times Y$ vector with all elements equal to one. Then, the HT can be implemented to $\mathbf{M}'(x,y)$ for m-D feature extraction.

As shown in Fig. 8(a), the simulation conditions are the same as those in Section IV-C1, and the body's returns are added with SNR $= -20$ dB. It can be found that the m-D curves are relatively very weak and that the HT may have errors when detecting the parameter pairs of curves. The result of the noise suppression processing is shown in Fig. 8(b). Applying the HT to this figure, the parameter pairs can accurately be detected.

However, similar with many other algorithms, the m-D extraction algorithm presented herewith cannot effectively work when the noise is overwhelming. As shown in Fig. 8(c), when the SNR decreases to -30 dB, the noise suppression does not effectively work, so that the curve with a frequency of 8 Hz can no longer be detected by HT. In this case, it is necessary to improve the noise suppression algorithm in future works.

When $A < c/(4N\Delta f)$ or the rotating rate is extraordinarily high, the Gabor transform or the STFT needs to be implemented before the HT. In these cases, the body's returns will bring in adverse effects because of the limitation of the time–frequency resolution. Therefore, the antinoise ability of the algorithm will be degraded to some extent. In particular, for the STFT, the multicomponent signal of the body's returns will seriously contaminate the m-D curves on the frequency-slow-time plane.

Fig. 9 shows the robustness of the proposed algorithm when $A < c/(4N\Delta f)$. The simulation conditions are the same as those in Section IV-C2, and SNR $= -16$ dB. The results of Gabor transform and the noise suppression processing are shown in Fig. 9(a) and (b), respectively, and the HT can accurately detect the parameters of the curves.

Fig. 10 shows the robustness of the algorithm when the rotating rate is extraordinarily high. The simulation conditions are the same as those in Section IV-C3, and SNR $= -10$ dB. Applying the HT to Fig. 10(c), the m-D features can successfully be extracted.

Time-varying complex scattering coefficients: It is highly possible that the scattering coefficients are time-varying complex values if the rotating scatterers have large radii or high frequencies. When the rotating scatterers have large radii, we directly detect the curves from the range-slow-time plane; therefore, the time-varying complex scattering coefficients just lead to the varying moduli of the curves. When the rotating rates of the scatterers are extraordinarily high, we detect the curves on the frequency (range)-slow-time plane after taking the STFT to each burst and stitching up the time–frequency planes in order, and in each burst time, the scattering coefficients can be considered as constants approximately. In such case, the time-varying complex scattering coefficients also just lead to the varying moduli of the curves on the frequency (range)-slow-time plane. Due to the robustness of the HT to the discontinuities of the pattern, the adverse effects of the curves' varying moduli are very limited.

Fig. 11 shows the curves on the range-slow-time plane, where the simulation conditions are the same as those in Section IV-C1. The moduli and phases of scattering coefficients randomly vary within [0, 1] and $[0, 2\pi]$, respectively. Applying the HT to Fig. 11, the parameter pairs of the curves can accurately be detected.

Fig. 12 shows the curves on the frequency (range)-slow-time plane, where the simulation conditions are identical to those

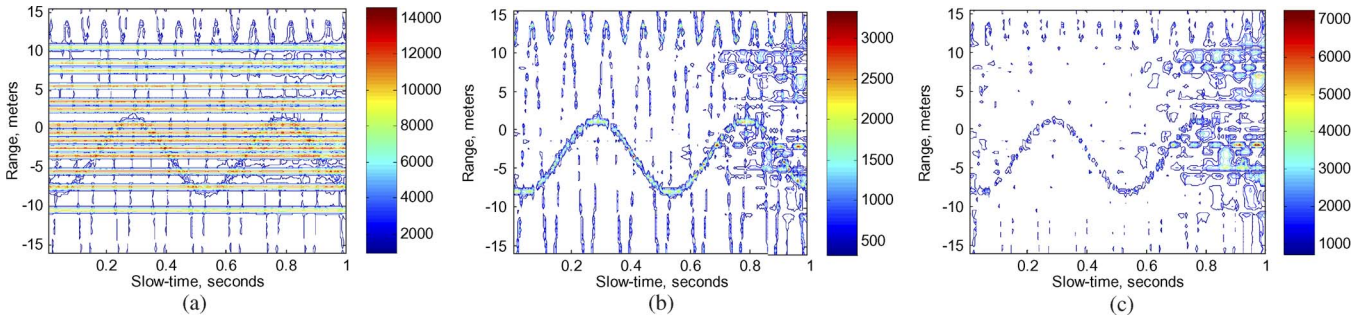

Fig. 8. Robustness validation of the proposed algorithm under different SNRs when detecting curves on the range-slow-time plane. (a) Curves and straight lines correspond to the micromotion scatterers and the body scatterers on the range-slow-time plane, respectively. The straight lines are considered as "noise" when extracting the m-D features. The SNR is -20 dB. (b) Result of the noise suppression processing when SNR $= -20$ dB. (c) Result of the noise suppression processing when SNR $= -30$ dB.

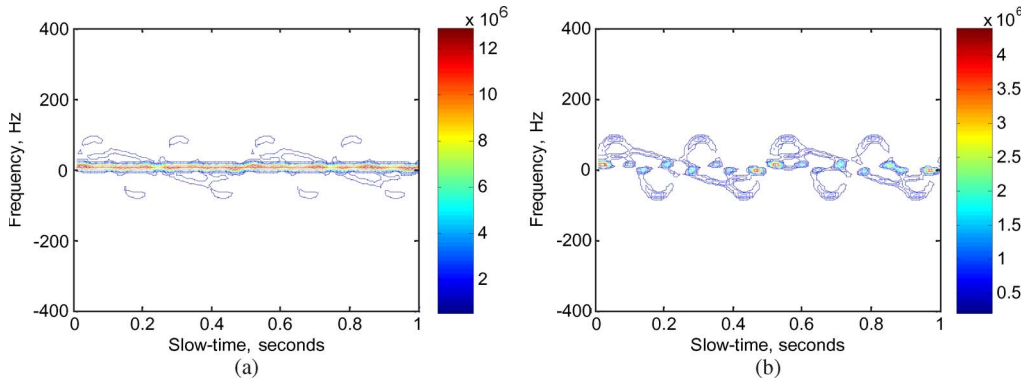

Fig. 9. Robustness validation when $A < c/(4N\Delta f)$ and SNR $= -16$ dB. (a) Result of Gabor transform. (b) Result of the noise suppression processing.

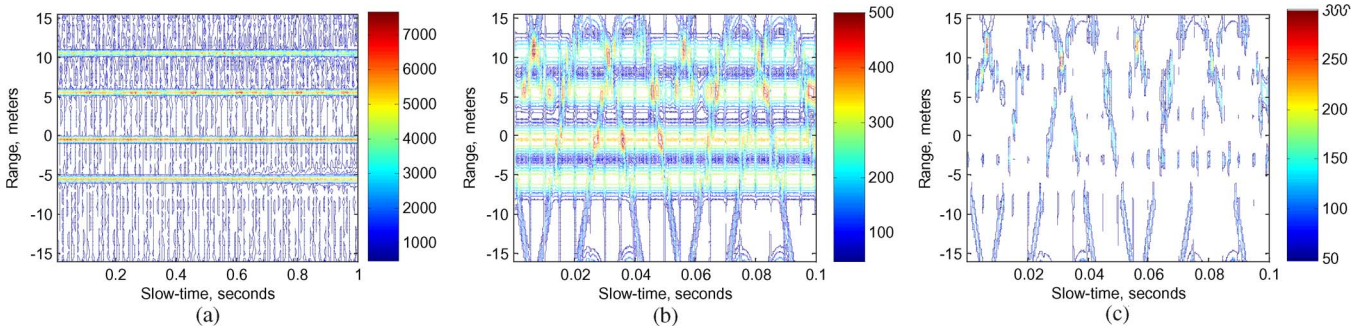

Fig. 10. Robustness validation when the rotating rate is extraordinarily high and SNR $= -10$ dB. (a) Blurry curves correspond to the micromotion scatterers, and straight lines correspond to the body scatterers on the range-slow-time plane. (b) New frequency (range)-slow-time plane constructed by stitching up the STFT results of all the bursts in order. (c) Result of the noise suppression processing.

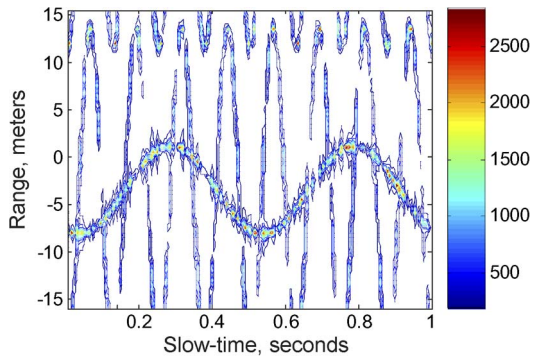

Fig. 11. Curves with time-varying complex scattering coefficients on the range-slow-time plane.

in Section IV-C3. The moduli and phases of scattering coefficients also randomly vary within [0, 1] and $[0, 2\pi]$, respectively. Applying the HT to Fig. 12, the parameter pairs of the curves can also accurately be detected.

From these analyses and simulations, it can be found that the proposed algorithm possesses good antinoise performance and robustness to the time-varying complex scattering coefficients.

V. Discussion and Conclusion

The m-D information has been verified to be very useful for radar target identification and recognition. In this paper, the m-D effects in SFCS radar have been investigated, and an algorithm for m-D signature extraction has been proposed.

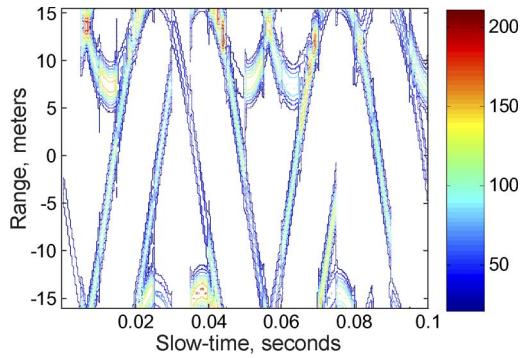

Fig. 12. Curves with time-varying complex scattering coefficients on the frequency (range)-slow-time plane after taking the STFT.

The proposed m-D signature extraction method is mainly based on the HT to detect the parameters of the curves on the range-slow-time plane or the frequency-slow-time plane. It is known that, when using the HT to detect patterns, the computer storage and the computational time exponentially grow with the number of dimensions in the parameter space [22]. The HT that we utilized here is a four-parameter mapping (when using the HT on the range-slow-time plane directly under the most common conditions or when the rotating rate is extraordinarily high) or a three-parameter mapping [when $A < c/(4N\Delta f)$]. In our simulation, the computation time for obtaining the parameter pairs (A', Ω, ζ) in Section IV-C2 was approximately 175 s on a personal computer with an Intel Pentium Dual T2330 (1.60 GHz) processor, whereas that for obtaining the parameter pairs (R_Q, A, Ω, ζ) from Fig. 7(c) was approximately 1311 s. In order to reduce the computation cost for real-time applications, some supplementary processing for speeding up the computation of the algorithm can be used, e.g., the fast method presented in [25] to detect fixed-period sinusoids based on the HT by decomposing the parameters into two groups and estimating them in turn can be extended to detect curves in this paper. The parallel processing technique can also be used to accelerate the computation of the HT.

It is mentioned that the main purpose of this paper is the m-D effect analysis and signature extraction in SFCS radars. In fact, based on the m-D signature extraction, the final ISAR image of the target body can be improved after eliminating the curves from the range-slow-time plane. The elimination algorithm for chirp radars has been discussed in our previous work [9], and it can also be extended to focus a clear body image in SFCS radars. Of course, considering the m-D characteristic differences between the chirp radar and the SFCS radar, the algorithm should be modified accordingly. For example, in this paper, the Gabor transform and STFT are adopted before the HT, and therefore, how the signals in range-slow-time domain could be reconstructed after curves eliminated from the time–frequency domain will be a subject for further research. The ISAR imaging algorithm based on the m-D signature extraction will be considered in a separate paper.

The simulations in Section IV have validated the accuracy of m-D effect analysis and the effectiveness of the proposed signature extraction algorithm. Due to the lack of the required real data, we can just examine the performance of the algorithm using simulated data at present. In our future work, we will introduce the algorithm to the real data processing.

REFERENCES

[1] V. C. Chen, "Analysis of radar micro-Doppler signature with time–frequency transform," in *Proc. Stat. Signal Array Process.*, Pocono Manor, PA, 2000, pp. 463–466.
[2] V. C. Chen, "Micro-Doppler effect of micromotion dynamics: A review," *Proc. SPIE*, vol. 5102, pp. 240–249, Apr. 2003.
[3] V. C. Chen, F. Li, S. S. Ho, and H. Wechsler, "Micro-Doppler effect in radar: Phenomenon, model, and simulation study," *IEEE Trans. Aerosp. Electron. Syst.*, vol. 42, no. 1, pp. 2–21, Jan. 2006.
[4] T. Sparr and B. Krane, "Micro-Doppler analysis of vibrating targets in SAR," *Proc. Inst. Elect. Eng.—Radar Sonar Navig.*, vol. 150, no. 4, pp. 277–283, Aug. 2003.
[5] T. Thayaparan, S. Abrol, E. Riseborough, L. Stankovic, D. Lamothe, and G. Duff, "Analysis of radar micro-Doppler signatures from experimental helicopter and human data," *IET Radar Sonar Navig.*, vol. 1, no. 4, pp. 289–299, Aug. 2007.
[6] J. Li and H. Ling, "Application of adaptive chirplet representation for ISAR feature extraction from targets with rotating parts," *Proc. Inst. Elect. Eng.—Radar Sonar Navig.*, vol. 150, no. 4, pp. 284–291, Aug. 2003.
[7] X. Bai, M. Xing, F. Zhou, G. Lu, and Z. Bao, "Imaging of micromotion targets with rotating parts based on empirical-mode decomposition," *IEEE Trans. Geosci. Remote Sens.*, vol. 46, no. 11, pp. 3514–3523, Nov. 2008.
[8] L. Stankovic, I. Djurovic, and T. Thayaparan, "Separation of target rigid body and micro-Doppler effects in ISAR imaging," *IEEE Trans. Aerosp. Electron. Syst.*, vol. 42, no. 4, pp. 1496–1506, Oct. 2006.
[9] Q. Zhang, T. S. Yeo, H. S. Tan, and Y. Luo, "Imaging of a moving target with rotating parts based on the Hough transform," *IEEE Trans. Geosci. Remote Sens.*, vol. 46, no. 1, pp. 291–299, Jan. 2008.
[10] S. He, Y. F. Zhu, H. Z. Zhao, J. X. Zhou, and F. Qiang, "Analysis of rotating structures for stepped frequency radar," in *Proc. Int. Conf. Radar*, 2008, pp. 386–390.
[11] A. Ghaleb, L. Vignaud, and J. M. Nicolas, "Micro-Doppler analysis of wheels and pedestrians in ISAR imaging," *IET Signal Process.*, vol. 2, no. 3, pp. 301–311, Sep. 2008.
[12] P. Setlur, M. Amin, and F. Ahmad, "Urban target classifications using time–frequency micro-Doppler signatures," in *Proc. 9th Int. Symp. Signal Process. Appl.*, 2007, pp. 1–4.
[13] Y. Kim and H. Ling, "Human activity classification based on micro-Doppler signatures using a support vector machine," *IEEE Trans. Geosci. Remote Sens.*, vol. 47, no. 5, pp. 1328–1337, May 2009.
[14] Q. Zhang and Y. Q. Jin, "Aspects of radar imaging using frequency-stepped chirp signals," *EURASIP J. Appl. Signal Process.*, vol. 2006, no. 13, pp. 85 823-1–85 823-8, 2006.
[15] A. Freedman, R. Bose, and B. D. Steinberg, "Thinned stepped frequency waveforms to furnish existing radars with imaging capability," *IEEE Aerosp. Electron. Syst. Mag.*, vol. 11, no. 11, pp. 39–43, Nov. 1996.
[16] N. Levanon and E. Mozeson, "Nullifying ACF grating lobes in stepped-frequency train of LFM pulses," *IEEE Trans. Aerosp. Electron. Syst.*, vol. 39, no. 2, pp. 694–703, Apr. 2003.
[17] Q. Zhang, Y. S. Zeng, Y. Q. He, and Y. Luo, "Avian detection and identification with high-resolution radar," in *Proc. IEEE Radar Conf.*, Rome, Italy, May 26–30, 2008, pp. 2194–2199.
[18] H. Schimpf, A. Wahlen, and H. Essen, "High range resolution by means of synthetic bandwidth generated by frequency-stepped chirps," *Electron. Lett.*, vol. 39, no. 18, pp. 1346–1348, Sep. 2003.
[19] R. T. Lord and M. R. Inggs, "High resolution SAR processing using stepped-frequencies," in *Proc. IEEE IGARSS*, Singapore, Aug. 1997, vol. 1, pp. 490–492.
[20] D. J. Rabideau, "Nonlinear synthetic wideband waveforms," in *Proc. IEEE Radar Conf.*, Long Beach, CA, May 2002, pp. 212–219.
[21] P. V. C. Hough, "Methods and means for recognizing complex patterns," U.S. Patent 3 069 654, Dec. 18, 1962.
[22] D. H. Ballard, "Generalization the Hough transform to detect arbitrary shapes," *Pattern Recognit.*, vol. 13, no. 2, pp. 111–122, 1981.
[23] D. S. Mckenzie and S. R. Protheroe, "Curve description using the inverse Hough transform," *Pattern Recognit.*, vol. 23, no. 3/4, pp. 283–290, Mar. 1990.
[24] S. Qian and D. Chen, "Discrete Gabor transform," *IEEE Trans. Signal Process.*, vol. 41, no. 7, pp. 2429–2438, Jul. 1993.
[25] Z. Changchun and S. Ge, "A Hough transform-based method for fast detection of fixed period sinusoidal curves in images," in *Proc. 6th Int. Conf. Signal Process.*, 2002, pp. 909–912.

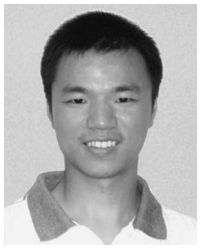

Ying Luo was born in Hunan, China, in 1984. He received the M.S. degree in electrical engineering, in 2008, from the Institute of Telecommunication Engineering, Air Force Engineering University (AFEU), Xi'an, China, where he is currently working toward the Ph.D. degree in electrical engineering. He is currently with the Radar and Signal Processing Laboratory, Institute of Telecommunication Engineering, AFEU. His research interests include signal processing and ATR in SAR and ISAR.

Qun Zhang (M'02–SM'07) received the M.S. degree in mathematics from Shaanxi Normal University, Xi'an, China, in 1988 and the Ph.D. degree in electrical engineering from Xidian University, Xi'an, in 2001. He was a Research Engineer from 2001 to 2003 and a Research Fellow from 2005 to 2006 with the Department of Electrical and Computer Engineering, National University of Singapore, Singapore. He is currently a Professor with the Telecommunication Engineering Institute, Air Force Engineering University, Xi'an, and an Adjunct Professor with the Key Laboratory of Wave Scattering and Remote Sensing Information (Ministry of Education), Fudan University, Shanghai, China. He has authored more than 100 papers on journals and conference proceedings. His research interests include signal processing, clutter suppression, and its application in SAR and ISAR.

Dr. Zhang is a Senior Member of the Chinese Institute of Electronics (CIE); a Committee Member of the Radiolocation Techniques Branch, CIE; and a member of the Signal Processing Council of Shaanxi, China. He was also a Vice Co-Chair of the Technical Program Committee of Workshop for Space, Aeronautical and Navigational Electronics in 2009. He was the recipient of the First-Grade and the Second-Grade Prizes of Shaanxi Natural Science Excellent Academic Paper in 2006 and 2008, respectively.

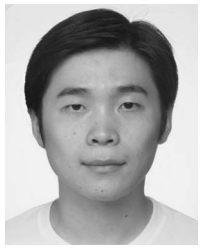

Cheng-wei Qiu (M'06) was born in Zhejiang, China, on March 9, 1981. He received the B.Eng. degree from the University of Science and Technology of China, Hefei, China, in 2003 and the Ph.D. degree from the Joint Ph.D. Program between the National University of Singapore, Singapore and the L'École Supérieure d'Électricité (SUPELEC), Gif-sur-Yvette, France, in 2007.

Since 2009, he has been a Postdoctoral Fellow with the Research Laboratory of Electronic, Massachusetts Institute of Technology, Cambridge, MA. He has authored more than 40 journal papers and one book chapter, and has given a few invited talks at conferences. His research interests include the electromagnetic wave theory of complex media (e.g., chiral, anisotropic, and bianisotropic materials), invisibility cloaks, metamaterials, and imaging.

Dr. Qiu was the recipient of the SUMMA Graduate Fellowship in Advanced Electromagnetics in 2005; the IEEE AP-S Graduate Research Award in 2006; the Young Scientist Travel Grant in Japan in 2007; the Travel Grant for Metamaterial '07 in Rome, Italy; and the URSI Young Scientist Award in 2008.

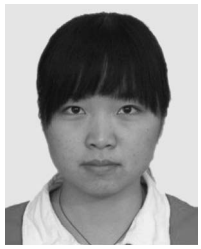

Xian-jiao Liang was born in Hunan, China, in 1986. She is currently working toward the M.S. degree in electrical engineering in the Institute of Telecommunication Engineering, Air Force Engineering University, Xi'an, China. Her research interests include signal processing in SAR and ISAR.

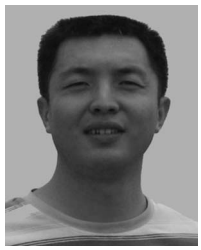

Kai-ming Li received the M.S. degree in electrical engineering from the Institute of Telecommunication Engineering, Air Force Engineering University (AFEU), Xi'an, China, in 2009. He is currently with the Radar and Signal Processing Laboratory, Institute of Telecommunication Engineering, AFEU. His research interests include signal processing and ATR in SAR and ISAR.